https://doi.org/10.5194/egusphere-2025-4639
Preprint. Discussion started: 6 October 2025

Comparative analysis of GOME and SCIAMACHY reflectance over Pseudo-Invariant Calibration Sites: implications for spectrometers cross-calibration

Abdalmenem Owda [1] and Günter Lichtenberg [1]

[1]Remote Sensing Technology Institute, German aerospace center (DLR), Weßling, Germany

Correspondence: Abdalmenem Owda (abdalmenem.owda@dlr.de)

Abstract. Accurate radiometric cross-calibration is essential for ensuring the consistency and interoperability of multi-sensor satellite observations. Vicarious calibration, a widely adopted approach, relies on the temporal stability of desert-based Pseudo-Invariant Calibration Sites (PICS). However, these sites are limited in spatial extent and have not been systematically examined for cross-calibration with larger pixels, whose dimensions exceed those of PICS. This study establishes a statistical framework to advance cross-calibration of spectrometers over PICS and their surrounding areas. The framework includes performance comparisons of different satellite instruments and the identification of reference and constrained sensors. Furthermore, the temporal stability of PICS across various spectral bands was reassessed using observations from the reference sensor. Stability scores (SS) were derived from a combination of statistical indicators designed to capture temporal variability, distribution symmetry, the occurrence of anomalies, and long-term shifts in the observations.

Decades of surface reflectance data in the ultraviolet, visible, and near-infrared (UV/VIS/NIR) ranges, collected by the Global Ozone Monitoring Experiment (GOME) and Scanning Imaging Absorption Spectrometers for Atmospheric Chartography (SCIAMACHY) spectrometers over 20 PICS sites, were analyzed. The results revealed significant degradation in GOME, particularly in the UV band during 2001 and toward the end of its mission, as evidenced by positively skewed and heavy-tailed distributions. In contrast, SCIAMACHY observations were more uniform and stationary, indicating their greater suitability for assessing PICS stability. The investigated sites were ranked based on the average of SS across the whole investigated spectrum. The analysis revealed a wide range of stability levels among PICS, including intra-site variations across spectral bands. While some sites demonstrated consistently high stability, many were found to be 2-3 times less stable than the most stable sites. Among these robust sites, some have not been recommended by the calibration communities and should be given further consideration. These findings underscore the importance of regularly evaluating PICS and the need to consider spectral-band-specific performance when selecting calibration sites.

1 Introduction

In recent decades, the number of satellite missions has significantly increased, leading to a paradigm shift across various applications. This expansion has resulted in an abundance of remote sensing data and a rapid growth in data archives. Long-term monitoring applications, such as those focused on atmospheric gases, require continuous time series data that often

https://doi.org/10.5194/egusphere-2025-4639
Preprint. Discussion started: 6 October 2025

extend beyond the operational lifespan of individual satellite missions (Cabor et al., 1998). Ensuring radiometric consistency among these datasets is critical for integrating observations from different satellite missions. Furthermore, it is fundamental for developing high data quality to perform quantitative remote sensing (Helder et al., 2013).

Various calibration strategies can be used to ensure consistency across both temporal and spectral domains, ranging from pre-flight (Lichtenberg et al., 2006; Coldewey-Egbers et al., 2008), in-flight calibration (Pagano et al., 2003; Ono et al., 1996), and vicarious calibration (Cabor et al., 1998; Wu et al., 2020; Helder et al., 2013; Chander et al., 2013; Ye et al., 2021). Notably, vicarious calibration is independent of the onboard calibration systems and provides an external means of validating and correcting satellite measurements.

Pseudo-invariant Calibration Sites (PICS) are among the most widely utilized targets in vicarious calibration methods (Kabir et al., 2020; Hasan et al., 2019), and absolute radiometric calibration (Helder et al., 2013). A set of 20 desert sites, each measuring 100 × 100 km^2, was proposed across Africa and the Arabian Peninsula in (Cosnefroy et al., 1996). Several of these sites have been recommended as reference calibration and validation test sites by the Committee on Earth Observation Satellites (CEOS), specifically by the Working Group on Calibration and Validation (WGCV) and the Infrared and Visible Optical Sensors (IVOS) (Thenkabail, 2015; Liang, 2017). As reported in (Cosnefroy et al., 1996), the spatial uniformity of these sites is better than 3% in relative terms, based on a multitemporal series of cloud-free images. Furthermore, the typical peak-to-peak temporal variation in reflectance was found to range between 8% and 15% in relative values.

PICS have been the subject of several recent studies (Khadka et al., 2021; Tuli et al., 2019; Fajardo Rueda et al., 2021; Hasan et al., 2019). These investigations confirmed that PICS remain relevant and reliable for radiometric calibration of optical remote sensing systems. Therefore, any radiometric deviations in the acquired scenes that exceed the expected temporal stability of PICS may suggest potential instrumental anomalies and necessitate further calibration or investigation—this principle forms the basis for employing PICS in radiometric calibration, sensor performance monitoring, and cross-calibration between different sensors.

While PICS are well-established in the radiometric and cross-calibration of optical sensors, their applications to spectrometer calibration remain largely unexplored. Spectrometers typically have a much larger spatial footprint than that of PICS. Therefore, the temporal stability of areas larger than the PICS domain should be assessed before their use in cross-calibration. To address this gap, this research paper aims to establish a foundation for spectrometer cross-calibration through two key objectives. The first objective is to develop a statistical framework for the comparative analysis of spectrometers, to monitor their performance throughout the mission lifetime, and identify both the reference and the constrained sensor. The second objective is to assess the temporal stability of PICS and surrounding areas across the full spectrum.

This study is based on two main hypotheses. The first hypothesis pertains to sensor performance, specifically that the reflectance samples are expected to follow a normal distribution under optimal sensor operating conditions. For the temporal variability of PICS, it is assumed that all PICS, owing to their common atmospheric and meteorological conditions, exhibit consistent patterns of temporal variability in surface reflectance, regardless of the observing sensors. Any deviations from this expected behavior may serve as an indicator of site-specific or sensor-related instability, thereby enabling the assessment of site reliability and the identification of the most suitable sensor to serve as a reference in the cross-calibration efforts.

https://doi.org/10.5194/egusphere-2025-4639
Preprint. Discussion started: 6 October 2025

The surface reflectance observations from the Global Ozone Monitoring Experiment (GOME) and Scanning Imaging Absorption Spectrometers for Atmospheric Chartography (SCIAMACHY) over the PICS were used in this study. A decade of data was used to extract reflectance time series across three spectral bands: ultraviolet (UV), visible (VIS), and near-infrared (NIR).

The paper is structured as follows: Section 2 describes the sensors and their data used in this investigation. Section 3 presents the geographical locations of the investigated PICS. The methods are presented in Section 4. Results and Discussions are presented in Sections 5 and 6. Finally, the Conclusion and Outlook in Section 7.

2 Sensor and data descriptions

2.1 GOME

GOME (1995–2011) was a passive nadir-scanning UV/VIS spectrometer onboard ERS-2 (ESA, 2025a). It provided global 3-day observations of ozone, NO_2, clouds, aerosols, and other atmospheric parameters over 240–790 nm. GOME had forward and backward scanning sequences with four pixels per scan. Forward scans included east, nadir, and west pixels at 40 $\times$ 320 km^2, while the backscan pixel had 40 $\times$ 920 km^2 resolution (Burrows et al., 1999).

2.2 SCIAMACHY

SCIAMACHY (2002–2012) was a passive UV/VIS/NIR imaging spectrometer on ENVISAT (ESA, 2025b), covering 240–2400 nm. It featured nadir, limb, and sun/moon occultation viewing; nadir spatial resolution ranged from 32 $\times$ 233 km^2 to 26 $\times$ 30 km^2 with a maximum swath of 960 km. Limb and occultation modes were excluded in this study. SCIAMACHY retrieved trace gases, aerosols, radiation, and cloud properties (Heinrich Bovensmann et al., 1999).

The differences between GOME and SCIAMACHY are illustrated in Table 1.

Table 1. Comparison of GOME and SCIAMACHY satellite instruments.

Item	GOME	SCIAMACHY
Mission life	1995–2011	2002–2012
Orbit	sun-synchronous, 790 km	sun-synchronous, 799.8 km
Overpassing time (local time)	10:30 am	10:00 am
Observation geometries	Nadir	Nadir, Limb, Occultation
Ground pixel size (km^2)	40×320	32×233 to 26×30
Number of channels	4	8
Total spectral range (nm)	237–793	212–2386
UV channel range / resolution (nm/nm)	311–405 / 0.17	300–412 / 0.26
VIS channel range / resolution (nm/nm)	405–611 / 0.29	383–628 / 0.44
NIR channel range / resolution (nm/nm)	595–793 / 0.33	595–812 / 0.48

https://doi.org/10.5194/egusphere-2025-4639
Preprint. Discussion started: 6 October 2025

2.3 GOME and SCIAMACHY data

The fully calibrated Level 1 products from GOME (Level 1b) and SCIAMACHY (Level 1c) were used to retrieve the reflectance time series. GOME Level 1b and SCIAMACHY Level 1c data contained solar irradiance and radiance measurements to compute reflectance. GOME Level 1b files provided cloud parameters. For SCIAMACHY, cloud parameters were only available in Level 2 products. For this study, we extracted the parameters from Level 2.

The following were the main data from both sensors used:

- Reflectance: This parameter refers to the fraction of incoming radiation reflected toward the instruments. This consists of surface reflectance and atmospheric scattering. Reflectance serves as a fundamental parameter for the comparison between sensors and the study of the temporal variability of PICS.
- Cloud fraction (CF): This parameter ranges from 0 to 1, where 0 indicates clear skies (no clouds) and 1 indicates full cloud cover. The cloud fraction is used to filter out data with a higher CF in the reflectance time series.
- Viewing geometry of spectrometers: The solar zenith angle (SZA) and viewing zenith angle (VZA) are geometric parameters that may influence the temporal variability of reflectance. SZA is the angle between the local vertical and the sun, and VZA is the angle between the local vertical and the satellite line of sight.

3 Study areas description

PICS are shown in Fig. 1, and are the selected sites for this study. These sites, located primarily in desert regions, were chosen due to their minimal vegetation cover and stable surface reflectance characteristics. These features make them particularly suitable for satellite sensor intercomparison and cross-calibration. Further details on the geographical locations of the PICS are provided in Table A1 in the Appendix.

https://doi.org/10.5194/egusphere-2025-4639
Preprint. Discussion started: 6 October 2025

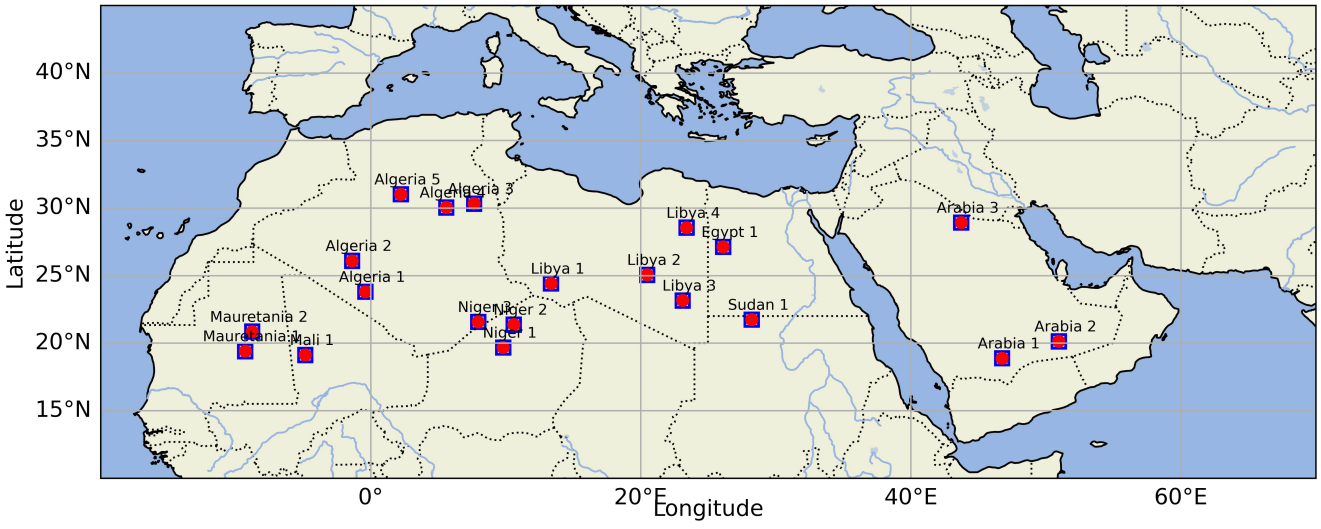

Figure 1. PICS in Africa and the Arabian Peninsula with the dimensions of 100 × 100 km^2.

https://doi.org/10.5194/egusphere-2025-4639
Preprint. Discussion started: 6 October 2025

4 Methods

This section outlines the methodological workflows, addressing the two key objectives of the study: (i) comparative assessment of GOME and SCIAMACHY across the PICS and investigated spectrum ranges, (ii) modeling SS for each PICS based on derived metric parameters.

4.1 Comparative assessment of GOME and SCIAMACHY

4.1.1 Computation of the reflectance

The reflectance measurements from both sensors were computed with the assumption of a Lambertian surface. The reflectance from GOME (R_g) and SCIAMACHY (R_s) were computed based on Eq. (1):

$$R(\lambda) = \frac{\pi . I_{earth}(\lambda)}{cos(\phi_o) . E_{sun}(\lambda))} \tag{1}$$

where $R(\lambda)$ is the reflectance as a function of wavelength, $I_{earth}(\lambda)$ is the calibrated radiance as measured by the instrument as a function of wavelength, ϕ_o is the solar zenith angle, and E_{sun} is the solar irradiance as measured by the instrument.

The effects of different SZA and VZA were investigated for SCIAMACHY reflectance before computation of the SS in Section 5.4.

4.1.2 Retrieving of time series of reflectance from GOME and SCIAMACHY

The reflectance data from the complete archival record of ESA's GOME and SCIAMACHY spectrometers over each PICS were retrieved. The retrieved reflectance data spanned spectral ranges in UV/VIS/NIR. The selected wavelength ranges and the corresponding number of spectral channels are presented in Table 2. For each satellite overpass, reflectance values were extracted within a $1.5° \times 1.5°$ bounding box centered over the PICS. This area was chosen to be larger than the actual PICS extent because the GOME pixel size exceeded the PICS dimensions, resulting in only a single reflectance value per overpass. In contrast, SCIAMACHY could provide multiple reflectance values within the PICS, and their average was used for analysis. We applied a threshold of CF ≤ 0.25 to filter the time series. This threshold was chosen to minimize the influence of cloud contamination on the observed reflectance values, as high CF can significantly alter the magnitude and variability of the measurements.

Table 2. Characteristics of the selected wavelength ranges for each spectral band, including the number of spectral channels corresponding to each band for the GOME and SCIAMACHY sensors.

Band	Selected wavelength range [nm]	Number of spectral channels in GOME	Number of spectral channels in SCIAMACHY
UV	309.45–391.74	705	758
VIS	423.92–526.93	494	436
NIR	753.97–775.91	105	106

https://doi.org/10.5194/egusphere-2025-4639
Preprint. Discussion started: 6 October 2025

4.1.3 Deriving temporal stability metrics

For each investigated PICS site (S_k) and wavelength (λ), we extracted a set of statistical and signal-based features that described the temporal variability of the reflectance time series. The extracted features offered a multidimensional representation of the reflectance dynamic for monitoring sensors' performance and identifying the stability of spectral channels and sites. The parameters were categorized into two different groups as follows:

1. *Basic statistics parameters*: These parameters include the mean (μ), the standard deviation (σ), the coefficient of variation (CV), and the interquartile range (IQR).
   μ describes the average reflectance over time (Eq. (2)), σ is used to describe the absolute temporal variability around the mean (Eq. (3)), CV describes the degree of variability in the reflectance time series (Eq. (4)). IQR measures the statistical dispersion in the middle range of 50 % of the dataset (Eq. (5)).
   For each site S_k and λ from a sensor $\mathcal{S}$ at time t_n, the reflectance time series was denoted as $R^{S_k}_{\mathcal{S},\lambda}(t_n)$

$$\mu^{S_k}_{\mathcal{S},\lambda} = \frac{1}{N}\sum_{n=1}^{N} R^{S_k}_{\mathcal{S},\lambda}(t_n) \tag{2}$$

$$\sigma^{S_k}_{\mathcal{S},\lambda} = \sqrt{\frac{1}{N}\sum_{n=1}^{N}\left(R^{S_k}_{\mathcal{S},\lambda}(t_n) - \mu^{S_k}_{\mathcal{S},\lambda}\right)^2} \tag{3}$$

$$\mathrm{CV}^{S_k}_{\mathcal{S},\lambda} = \frac{\sigma^{S_k}_{\mathcal{S},\lambda}}{\mu^{S_k}_{\mathcal{S},\lambda}} \tag{4}$$

$$\mathrm{IQR}^{S_k}_{\mathcal{S},\lambda} = Q_3\left(R^{S_k}_{\mathcal{S},\lambda}\right) - Q_1\left(R^{S_k}_{\mathcal{S},\lambda}\right) \tag{5}$$

   where N is the number of observations for each reflectance time series. The number of observations for each site is tabulated in Table A1 in the Appendix. Q_3 is the 75th percentile, and Q_1 is the 25th percentile.

2. *Trend and shape parameters*: These parameters include the slope (m), the skewness (${\gamma_1}^{S_k}_{\mathcal{S},\lambda}$), and the kurtosis (${\gamma_2}^{S_k}_{\mathcal{S},\lambda}$) of the reflectance time series. The slope was estimated by fitting the reflectance to the linear regression model (Eqs. (6-7)). It describes the long-term changes and trends in the reflectance over time. γ_1 detects asymmetry in the reflectance distribution and gives insights about the anomaly (Eq. (8)). γ_2 measures the tailedness of the distribution (Eq. (9)).

$$R^{S_k}_{\mathcal{S},\lambda}(t_n) = a^{S_k}_{\mathcal{S},\lambda} t_n + b^{S_k}_{\mathcal{S},\lambda} + \varepsilon_n \tag{6}$$

https://doi.org/10.5194/egusphere-2025-4639
Preprint. Discussion started: 6 October 2025

$$m = a_{\mathcal{S},\lambda}^{S_k} \tag{7}$$

$$\gamma_1{}_{\mathcal{S},\lambda}^{S_k} = \frac{1}{N}\sum_{n=1}^{N}\left(\frac{R_{\mathcal{S},\lambda}^{S_k}(t_n) - \mu_{\mathcal{S},\lambda}^{S_k}}{\sigma_{\mathcal{S},\lambda}^{S_k}}\right)^3 \tag{8}$$

$$\gamma_2{}_{\mathcal{S},\lambda}^{S_k} = \frac{1}{N}\sum_{n=1}^{N}\left(\frac{R_{\mathcal{S},\lambda}^{S_k}(t_n) - \mu_{\mathcal{S},\lambda}^{S_k}}{\sigma_{\mathcal{S},\lambda}^{S_k}}\right)^4 \tag{9}$$

4.2 Computing stability score

4.2.1 Refinement reflectance observations

To ensure SS reliably represents the temporal variability of the sites, the following steps were applied:

- Exclusion of the absorption bands: The spectral channels that were strongly influenced by atmospheric absorption, for example, the O_2-A band, were excluded from the SS calculation.
- Normalization for illumination and viewing geometry: It is expected that a part of the variability in reflectance arises from differences in solar illumination and satellite viewing geometry. Therefore, the reflectance observations were corrected through SZA and VZA normalization. The reflectance dependence on SZA and VZA was quantified using regression analysis, and the resulting slopes were applied to normalize all observations to a fixed reference angle, as follows:

$$R_{\mathcal{S},\lambda}^{S_k}(t_n)_{\text{corr}} = R_{\mathcal{S},\lambda}^{S_k}(t_n) - m \cdot (\text{SZA} - \text{SZA}_{\text{ref}}) \tag{10}$$

  where $R_{\mathcal{S},\lambda}^{S_k}(t_n)_{\text{corr}}$ is the corrected reflectance, $R_{\mathcal{S},\lambda}^{S_k}(t_n)$ is the original observations before the correction, m is the slope, and SZA_{ref} is reference SZA, i.e, 45.

4.2.2 Parameterization of the stability score for each site

After retrieving the reflectance time series, heat maps were generated for the PICS. For each spectral channel, the corresponding parameters were derived and are presented in Table 3. These parameters were selected to estimate the spectral stability SS of each PICS (see Fig. 2). The reason for choosing these parameters was given in the same table. All selected parameters shared the same stability indicator, where lower values correspond to higher temporal stability.

The selected parameters for each time series of a wavelength were normalized based on Min-Max scaling (Han et al., 2022), shown in Eq. (11). The scaled parameters were in the range of 0 to 1.

https://doi.org/10.5194/egusphere-2025-4639
Preprint. Discussion started: 6 October 2025

$$\tilde{F} = \frac{F - F_{\min}}{F_{\max} - F_{\min}} \tag{11}$$

where F refers to the statistical parameters in Table 3. For each spectral channel, $\tilde{F}$ is the normalized parameter. SS was computed based on Eq. (12), in which the weight of parameters was equal for all.

$$SS^{S_k}_{\mathcal{S},\lambda} = \sum_{k=1}^{K} w_k \tilde{F}_k, \qquad \text{with} \quad \sum_{k=1}^{K} w_k = 1, \qquad \text{and} \quad w_k = \frac{1}{k} \tag{12}$$

where K is the number of features.

The overall SS of a PICS was represented by the average of $SS^{S_k}_{\mathcal{S},\lambda}$ of the whole spectrum (see the illustrative diagram (Fig. 2)).

$$\overline{SS^{S_k}_{\mathcal{S}}} = \frac{1}{N} \sum_{j=1}^{N} SS^{S_k}_{\mathcal{S},\lambda} \tag{13}$$

Table 3. Summary of statistical parameters used for temporal stability assessment of the PICS and their physical interpretation in evaluating the stability of reflectance time series.

Parameters	Physical interpretation in temporal stability	Stability indicator
$\sigma^{S_k}_{\mathcal{S},\lambda}$	A high $\sigma_{\mathcal{S},\lambda}$ indicates high temporal variability in the time series of reflectance	Low $\sigma_{\mathcal{S},\lambda} \rightarrow$ more stable
$\mathrm{CV}^{S_k}_{\mathcal{S},\lambda}$	A high $\mathrm{CV}^{S_k}_{\mathcal{S},\lambda}$ suggests an unstable pattern of the reflectance time series	Low $\mathrm{CV}^{S_k}_{\mathcal{S},\lambda} \rightarrow$ more stable
$\mathrm{IQR}^{S_k}_{\mathcal{S},\lambda}$	A high $\mathrm{IQR}^{S_k}_{\mathcal{S},\lambda}$ indicates high variability in the middle range of the reflectance time series	Low $\mathrm{IQR}^{S_k}_{\mathcal{S},\lambda} \rightarrow$ more stable
m	m describes the stationary status of the reflectance time series	Low $m \rightarrow$ more stable (stationary)
$\gamma_1{}^{S_k}_{\mathcal{S},\lambda}$	A high $\gamma_1{}^{S_k}_{\mathcal{S},\lambda}$ means more anomalies and asymmetry in the reflectance time series	Low $\gamma_1{}^{S_k}_{\mathcal{S},\lambda} \rightarrow$ more stable
$\gamma_2{}^{S_k}_{\mathcal{S},\lambda}$	A high $\gamma_2{}^{S_k}_{\mathcal{S},\lambda}$ suggests frequent extreme changes (spikes)	Low $\gamma_2{}^{S_k}_{\mathcal{S},\lambda} \rightarrow$ more stable

https://doi.org/10.5194/egusphere-2025-4639
Preprint. Discussion started: 6 October 2025

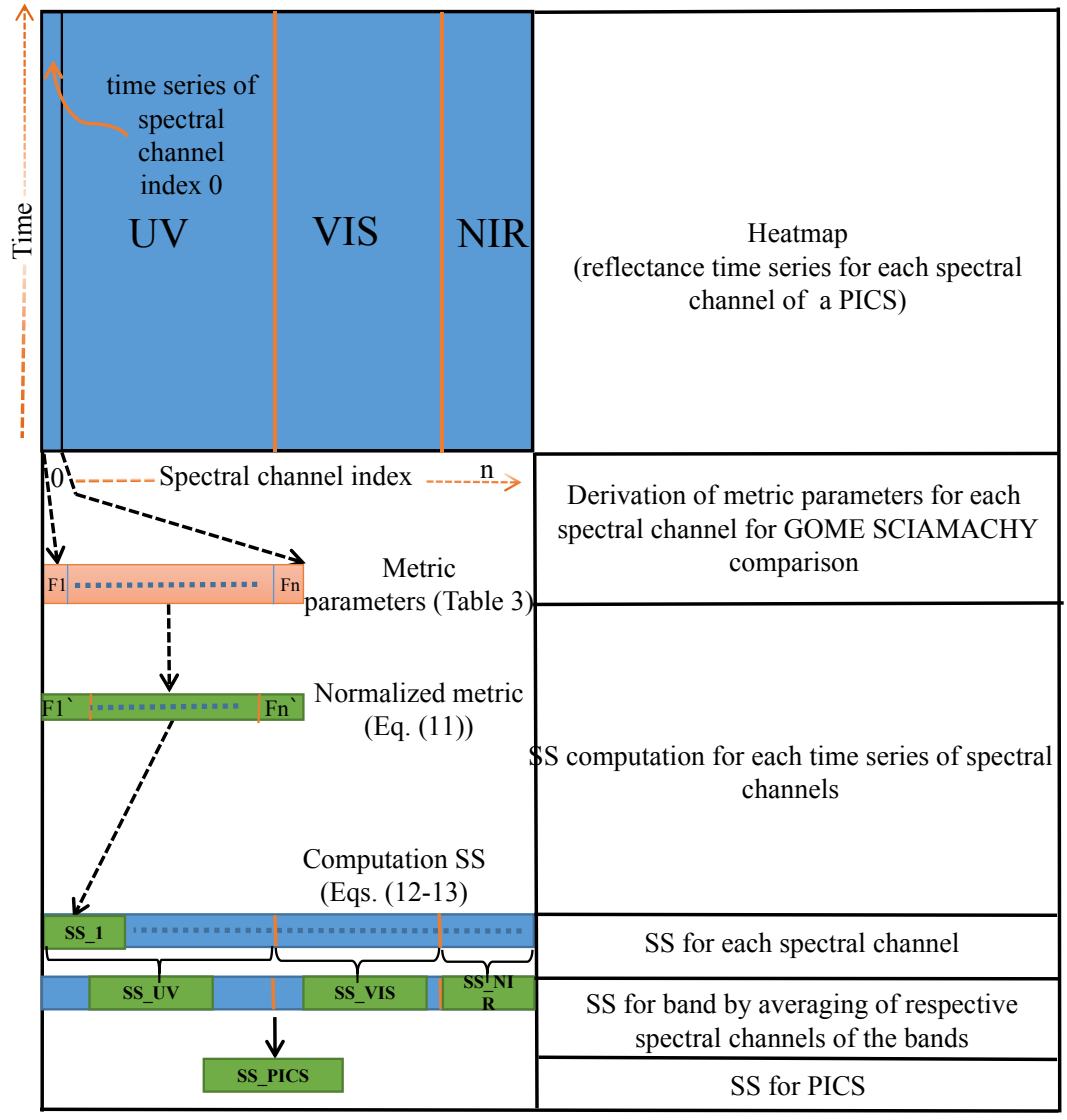

Figure 2. Methodological framework outlining the key steps: retrieval of reflectance time series, derivation of temporal metric parameters for each spectral channel, computation of SS per channel, band-wise averaging of spectral channels, and derivation of the final SS for each PICS site. The workflow of the computation of SS is shown for one spectral channel. The process is iterative across all spectral channels.

https://doi.org/10.5194/egusphere-2025-4639
Preprint. Discussion started: 6 October 2025

5 Results

5.1 GOME and SCIAMACHY reflectance time series of PICS

The reflectance time series of the PICS were retrieved under conditions of CF less than 0.25. Libya 4, one of the PICS endorsed by CEOS, WGCV, and IVOS, has been extensively used in previous studies for long-term stability assessments and sensor calibration (Lacherade et al., 2013; Barsi et al., 2018; Khadka et al., 2021; Helder et al., 2013). As a representative example, Libya 4 was selected for detailed visualization of the reflectance time series obtained from the GOME and SCIAMACHY sensors.

Figs. 3-4 present the corresponding heatmaps of reflectance measurements from GOME and SCIAMACHY, respectively. At certain points in time for GOME (Fig. 3), higher values of the reflectance were observed across the whole spectrum (horizontal bright lines). In the UV, the value of the reflectance exceeded the average value due to instrument degradation, particularly towards the end of the GOME mission in 2011. The VIS and NIR spectral ranges were more uniform. In the NIR spectral range, O_2 A-band was visible with low reflectances around the center of the band. Similar behavior was observed for SCIAMACHY as shown in Fig. 4. The main difference was the absence of larger variations over long periods in the UV, suggesting less degradation compared with GOME.

To gain further insight into the variability of the reflectance time series observed in the heatmaps, three wavelengths were selected. These wavelengths, located approximately at 330 nm (UV), 650 nm (VIS), and 770 nm (NIR), were indicated by white dashed lines in the heatmaps. Figs. 5–6 show the corresponding reflectance time series at these wavelengths, derived from GOME and SCIAMACHY data, respectively.

The reflectance time series at the UV wavelength of GOME at 329.5 nm exhibited significant fluctuations, with approximately 47% of the observations within $\pm 10\%$ of the average value. A noticeable increase in reflectance was observed in 2001 and toward the end of the GOME mission due to degradation effects (see Fig. 5). In contrast, the selected wavelengths in the VIS (436.47 nm) and NIR (736.19 nm) regions demonstrated greater consistency, with 87% and 96% of the observations, respectively, remaining within $\pm 10\%$ of their average values. Among them, the VIS wavelength showed a particularly more consistent pattern.

For SCIAMACHY, the average reflectance values at the corresponding wavelengths were comparable to those from GOME (see Fig. 6). A similar fluctuation pattern was observed in the UV band (329.98 nm), about 58.3% of observations were within $\pm 10\%$. Additionally, sinusoidal-like patterns were more apparent in the SCIAMACHY UV time series than in GOME. The reflectance series for the selected VIS (449.94 nm) and NIR (770.04 nm) wavelengths appeared even more consistent than those of GOME, with no evident degradation effects over the mission period.

https://doi.org/10.5194/egusphere-2025-4639
Preprint. Discussion started: 6 October 2025

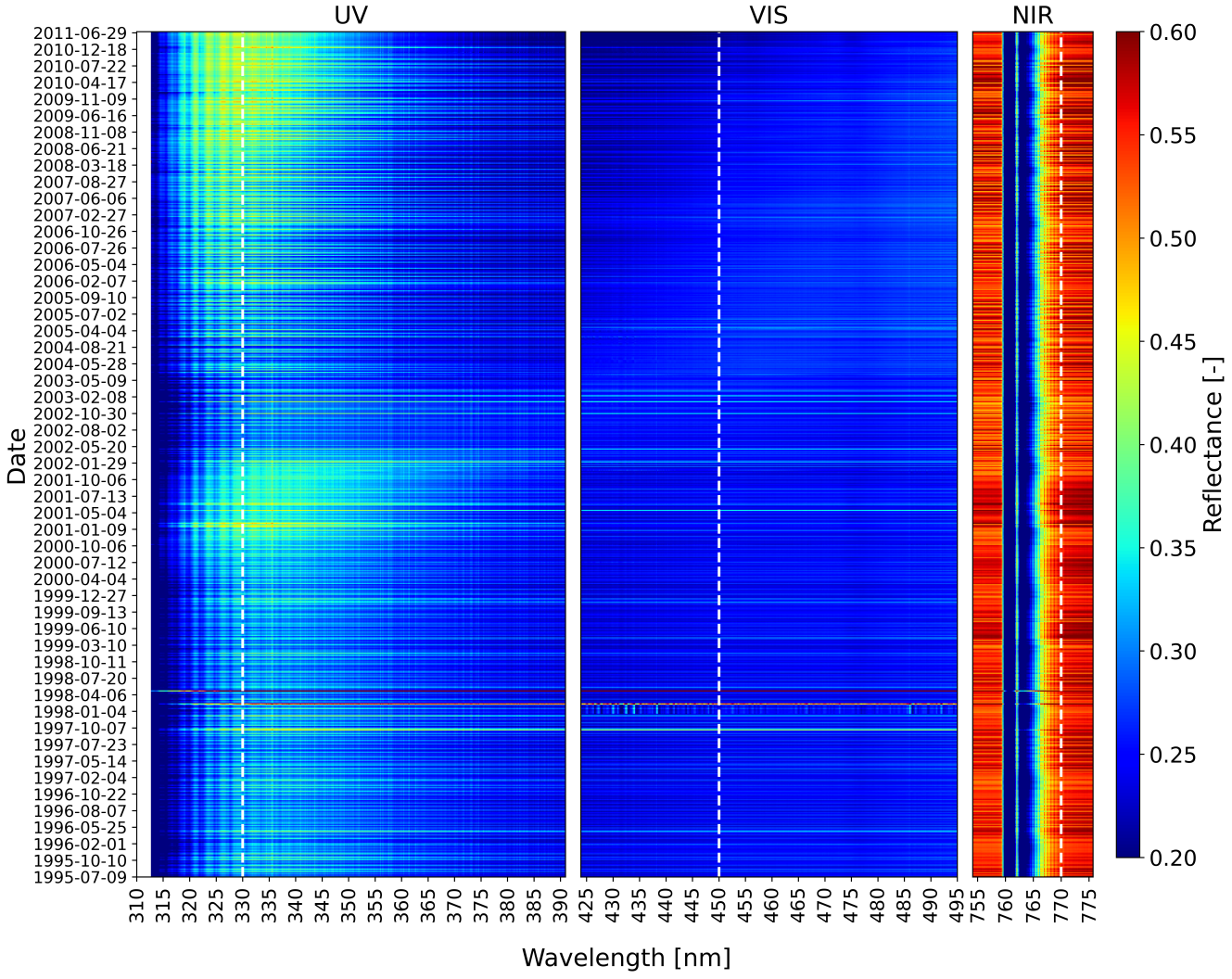

Figure 3. Heatmap of the GOME reflectance observations ($N = 716$) over Libya4. Three representative wavelengths from the UV, VIS, and NIR regions are highlighted with white dashed lines, and their time series are shown in Fig. 5.

https://doi.org/10.5194/egusphere-2025-4639
Preprint. Discussion started: 6 October 2025

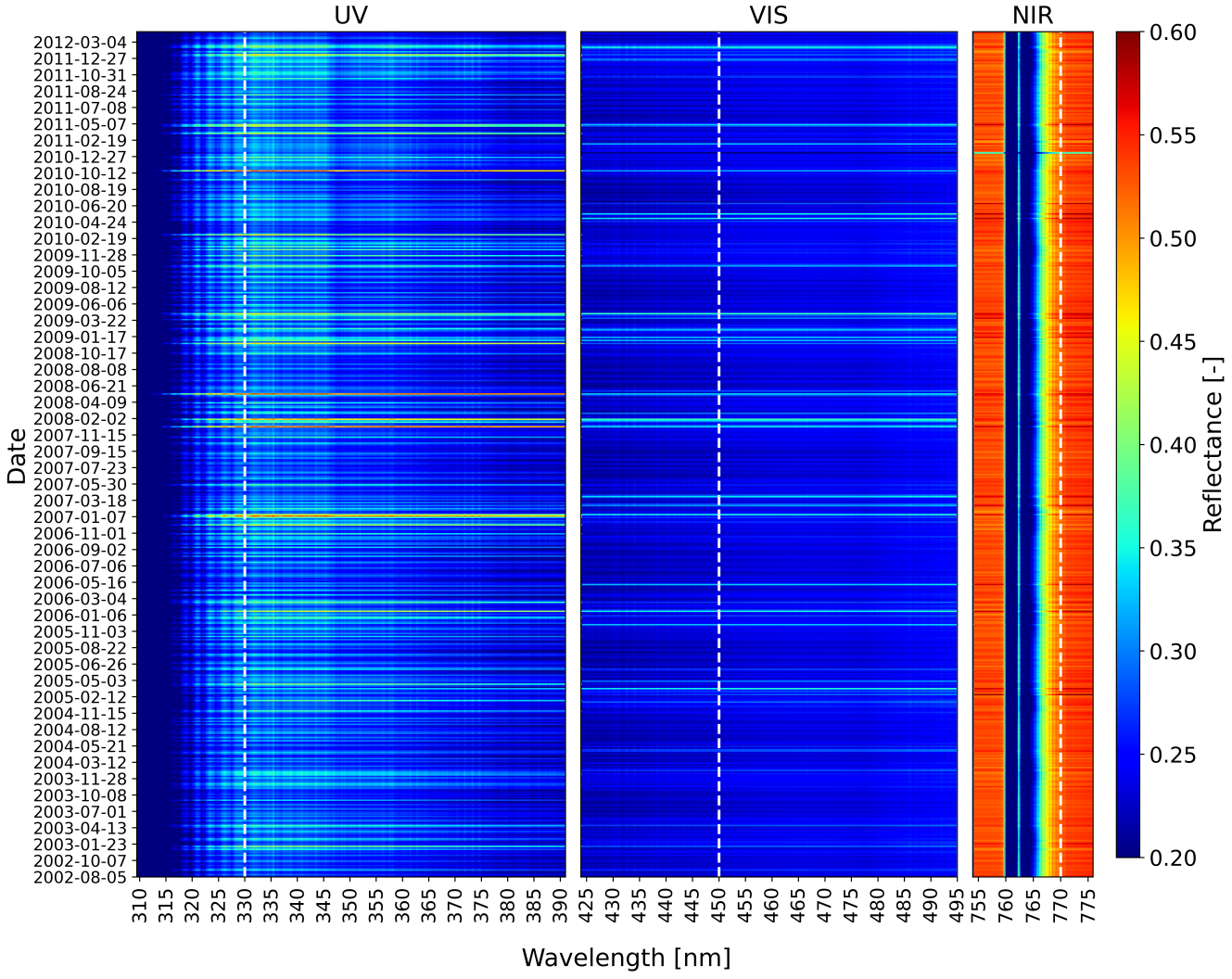

Figure 4. Same as in Fig. 3 but for SCIAMACHY reflectance observations ($N = 568$) and the time series of the selected wavelengths are shown in Fig. 6.

https://doi.org/10.5194/egusphere-2025-4639
Preprint. Discussion started: 6 October 2025

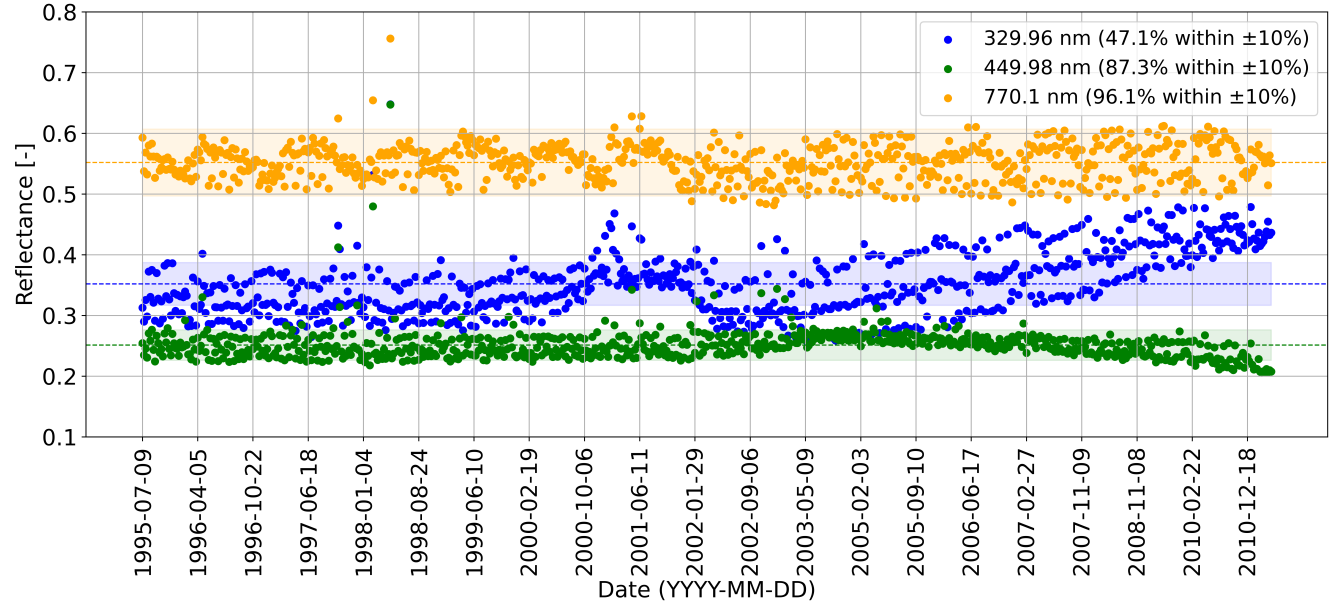

Figure 5. The reflectance time series of the wavelengths: 329.96 nm in UV (blue), 449.98 nm in VIS (green), and 770.10 nm in NIR (orange) from GOME with ($N = 716$).

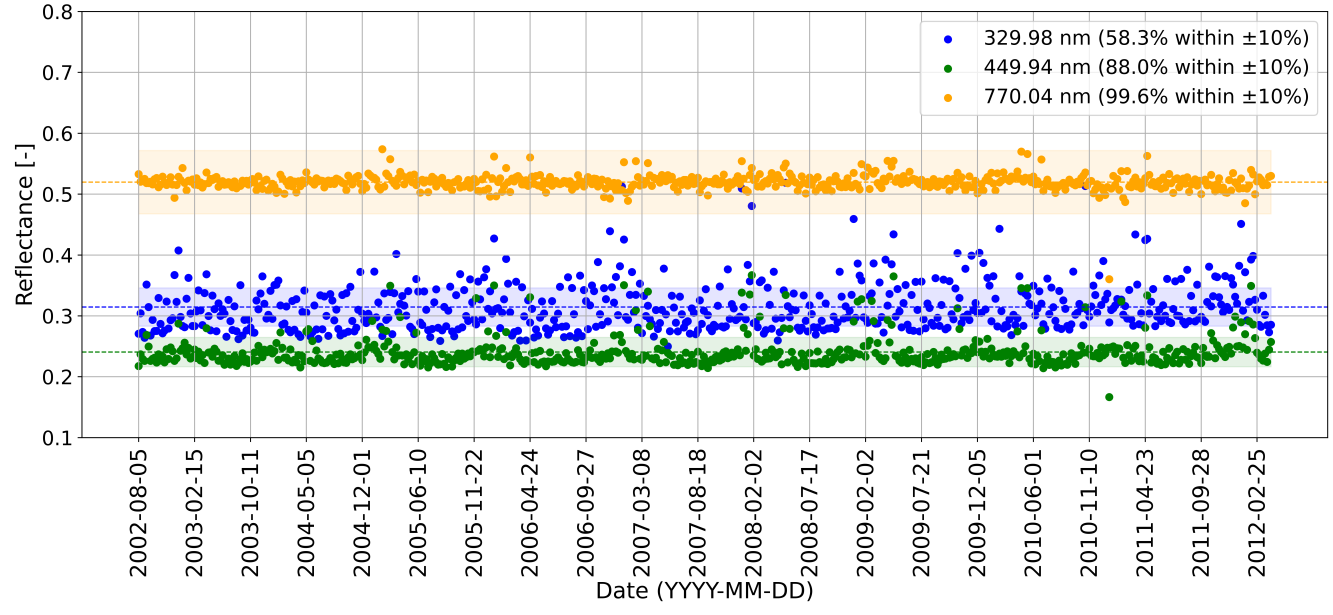

Figure 6. The reflectance time series of the wavelengths: 329.98 nm in UV (blue), 449.94 nm in VIS (green), and 770.04 nm in NIR (orange) from SCIAMACHY with ($N = 568$).

https://doi.org/10.5194/egusphere-2025-4639
Preprint. Discussion started: 6 October 2025

5.2 Temporal metrics from GOME and SCIAMACHY reflectance time series

The derived temporal metrics of the GOME and SCIAMACHY reflectance time series of each spectral channel from the investigated PICS are presented in Figs. 7-8. These results offered a comprehensive comparison of statistical features across the PICS sites and spectral channels.

The mean of the GOME reflectance time series in Fig. 7a demonstrated relatively low reflectance values in UV and VIS and higher reflectance values near the O_2 absorption window (O_2 A-band). The standard deviation in Fig. 7b and IQR in Fig. 7d showed higher UV variability for most sites. However, tighter spreads of the IQR were observed in VIS (see Fig. 7d). The CV in Fig. 7c showed notably higher values and a wide range across spectral channels and sites. The CV values were suddenly increased in the O_2 A-band. This was likely due to the low mean reflectance value in the absorption window. The slope values in Fig. 7e showed a notable pattern of degradation across most of the sites, particularly for the short wavelengths in UV. Smaller degradation patterns were observed in the VIS and NIR ranges. GOME reflectance time series demonstrated large magnitudes of Skewness in Fig. 7f and Kurtosis in Fig. 7g, suggesting higher variability and asymmetry across the spectral channels, especially in the O_2 A-band in NIR, which could be due to the influence of the clouds.

The mean reflectance values of SCIAMACHY were similar to GOME and showed similar patterns across all sites in Fig. 8a. There were relatively low reflectance values in UV and VIS, and higher reflectance values in NIR near the O_2 A-band. Low reflectance values were observed within the O_2 A-band (759–763 nm), indicating strong atmospheric absorption. The standard deviation in Fig. 8b and the IQR in Fig. 8d provided insights into the temporal variability of reflectance. Higher values in the UV range suggested greater fluctuations and noise, while lower values were in the VIS and on both sides of the O_2 A-band in NIR. The CV in Fig. 8c revealed differing levels of stability across spectral bands and among the PICS sites. In the UV, CV tends to increase with wavelength, while in the VIS, it remains relatively consistent. High CV values in the O_2 A-band in the NIR. Overall, the results suggested greater temporal stability in the VIS and spectral channels adjacent to the O_2 A-band compared to the UV. CV values among the sites range between 0.05 (5%) and 0.20 (20%). The slope values in Fig. 8e, especially in the UV, showed slight changes in the spectral signature of the sites. In contrast, many PICS sites exhibited slope values close to zero in the VIS and NIR, suggesting negligible long-term trends and stable reflectance behavior in these regions. The skewness values in Fig. 8f varied among sites and bands but remained consistent, reflecting differing degrees of asymmetry in the reflectance distributions. The VIS region exhibited more symmetric reflectance distributions compared to the UV. In the NIR, the absorption feature caused noticeable disruptions in symmetry. Similarly, kurtosis values in Fig. 8g, especially in the UV and NIR, suggested the presence of occasional outliers or extreme values. The VIS region, in contrast, showed fewer such anomalies.

The comparative analysis of temporal metrics for GOME and SCIAMACHY reflectance revealed different sensor performances and varying patterns across both PICS sites and spectral bands. Before assessing the stability of PICS, it is essential to first identify the most stable sensor data to be used in the analysis.

https://doi.org/10.5194/egusphere-2025-4639
Preprint. Discussion started: 6 October 2025

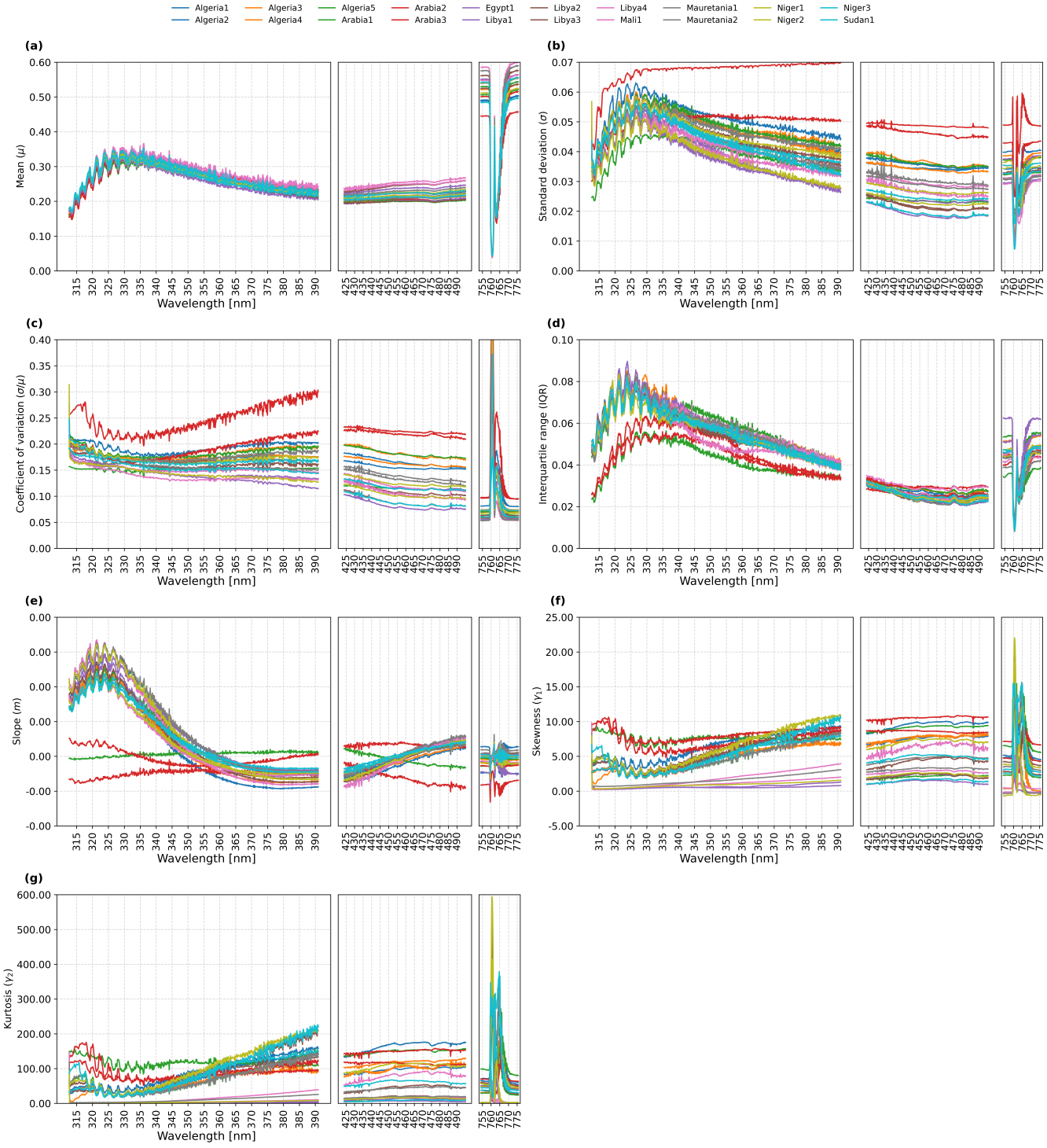

Figure 7. Temporal metrics of GOME reflectance time series of the investigated PICS include mean, standard deviation, coefficient of variation, interquartile range, slope, skewness, and kurtosis. Each subplot consists of three boxes, which refering to the wavelength ranges in UV/VIS/NIR.

https://doi.org/10.5194/egusphere-2025-4639
Preprint. Discussion started: 6 October 2025

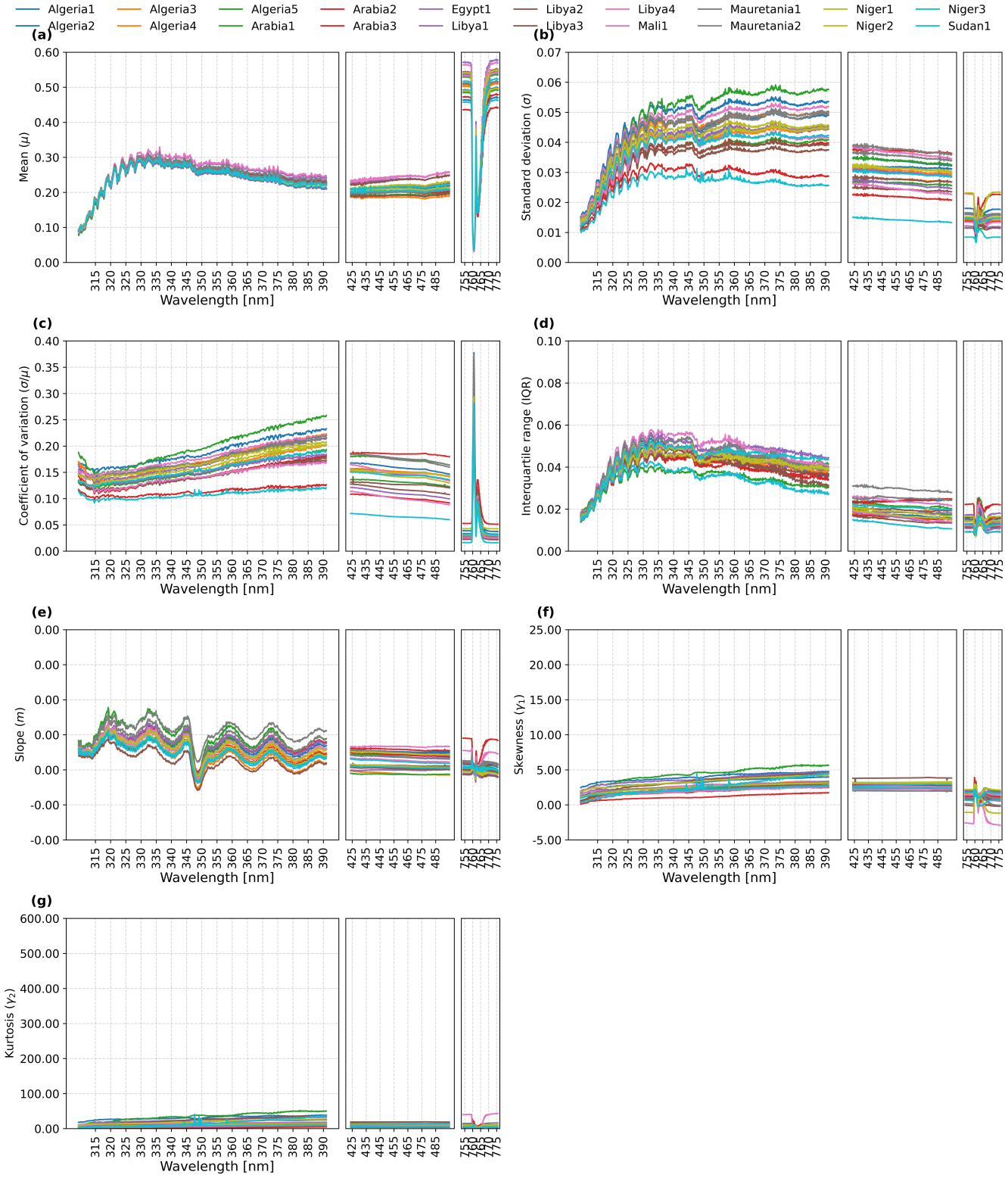

Figure 8. Same as in Figure 7 but for SCIAMACHY reflectance time series.

https://doi.org/10.5194/egusphere-2025-4639
Preprint. Discussion started: 6 October 2025

Table 4. Comparison of the average of metric temporal parameters for the investigated PICS.

Parameters	GOME	SCIAMACHY
Mean reflectance	Consistent patterns across all the sites; higher in NIR than in UV and VIS.	Very similar to GOME, with closely matching mean values across all sites.
Standard deviation	Higher variability in the UV band; lower values in VIS and NIR across all sites.	Same overall pattern but with systematically lower variability than GOME.
Interquartile range	Higher IQR in UV than in VIS and NIR across all sites.	Same spectral pattern as GOME, but with smaller IQR values.
Coefficient of variations	Higher CV in UV than in VIS and NIR for most PICS, indicating greater relative variability.	Matches GOME's spectral pattern but with lower CV magnitudes at all sites.
Skewness	Generally positive skew across sites. For some sites, VIS showing the largest skew compared to UV and NIR.	Lower skewness overall compared with GOME, indicating more symmetric reflectance distributions.
Kurtosis	Pronounced peaks—especially in VIS of some sites—suggesting occasional extreme reflectance events at some sites.	Flatter kurtosis curves (fewer extremes), with values consistently lower than those of GOME.
Slope	Shows larger slope magnitudes, suggesting possible sensor drift over time.	Near-zero slopes and very consistent across all sites, reflecting minimal long-term drift.

5.3 GOME Versus SCIAMACHY: a comparative analysis

The averages of the metric temporal parameters of each spectral band and site are shown in Fig. 9. The average values were computed by taking the mean of the parameters across the wavelength ranges defined for each band in Table 2. Key findings from these temporal metrics for both sensors are presented in Table 4. It presents the comparison of GOME and SCIAMACHY for each extracted parameter of each band.

GOME and SCIAMACHY shared several characteristics, particularly in their mean reflectance profiles. Both sensors exhibited similar reflectance patterns across the spectral channels (Fig. 9a). While both sensors displayed high temporal variability in the UV band, they maintained low variability across the VIS band.

However, GOME consistently displayed higher temporal variability and drift indicators than SCIAMACHY. Specifically, GOME's standard deviation, IQR, and CV were relatively higher (Fig. (9b-d)); its slope values suggested greater sensor drift (Fig. 7e); skewness was more strongly positive across most sites (Fig. 9f); kurtosis revealed more frequent extreme reflectance events (Fig. 9g). Collectively, these findings recommend adopting SCIAMACHY as the primary reference sensor for PICS stability assessments.

https://doi.org/10.5194/egusphere-2025-4639
Preprint. Discussion started: 6 October 2025

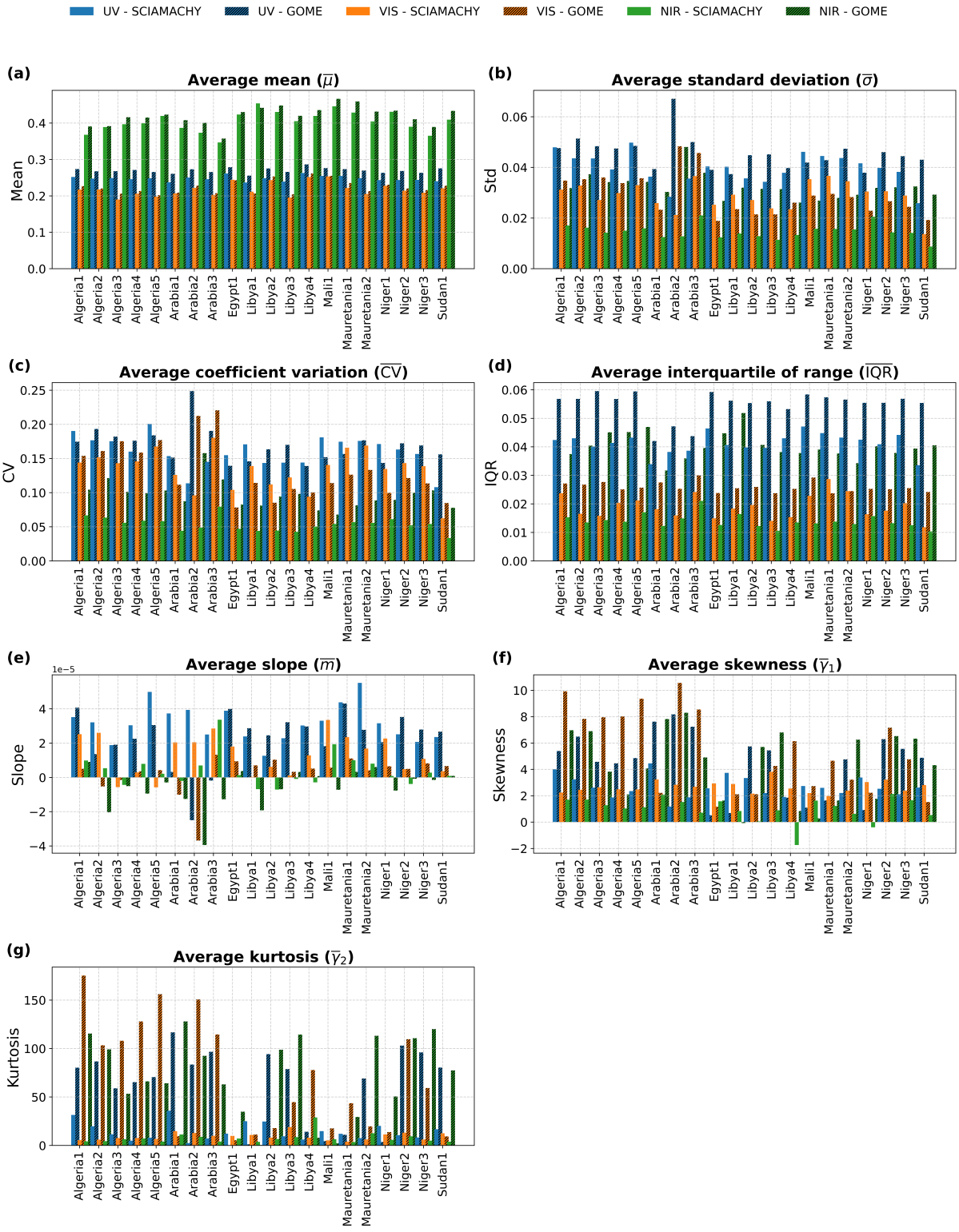

Figure 9. Average of metric temporal parameters for the investigated PICS. For each PICS site and sensor, three bars represent the metric values in the UV, VIS, and NIR bands (blue, orange, and green, respectively). Solid bars denote SCIAMACHY results, while hatched bars denote GOME.

https://doi.org/10.5194/egusphere-2025-4639
Preprint. Discussion started: 6 October 2025

5.4 Assessing solar and viewing geometry on SCIAMACHY reflectance

The mean reflectance across the full spectrum (UV/VIS/NIR) was first computed. Figs. 10a–b illustrate the relationships between the mean reflectance and the SZA and VZA. The results, summarized in Fig. 10c, indicate that mean reflectance typically varies by 1–2.5% per 10° increment in SZA, with a few sites, such as Arabia1 and Niger1, exhibiting lower sensitivity of approximately 0.5%. In contrast, the influence of VZA was minor, on the order of 0.5%. Overall, the findings suggest that mean reflectance is more sensitive to variations in SZA than in VZA. Based on these results, the reflectance observations of the PICS were corrected for SZA. The regression analysis of mean reflectance values revealed a systematic dependence on solar illumination geometry. To correct for this effect, the regression was performed separately for each spectral channel, ensuring that the dependence was adjusted on a channel-by-channel basis.

As an illustrative example, the reflectance differences for the Libya4 site (corrected - original) are provided in the Appendix (see Fig. A1).The effect of the correction was strongest in the UV spectral channels, weaker in the VIS channels, and smallest in the NIR region. The correction applied to the reflectance time sereis exhibited a clear sesonal dependence with the largest correction values for the reflectance time series of the summer months (May-September). Overall, the required adjustments were minor, with magnitudes on the order of 0.05.

https://doi.org/10.5194/egusphere-2025-4639
Preprint. Discussion started: 6 October 2025

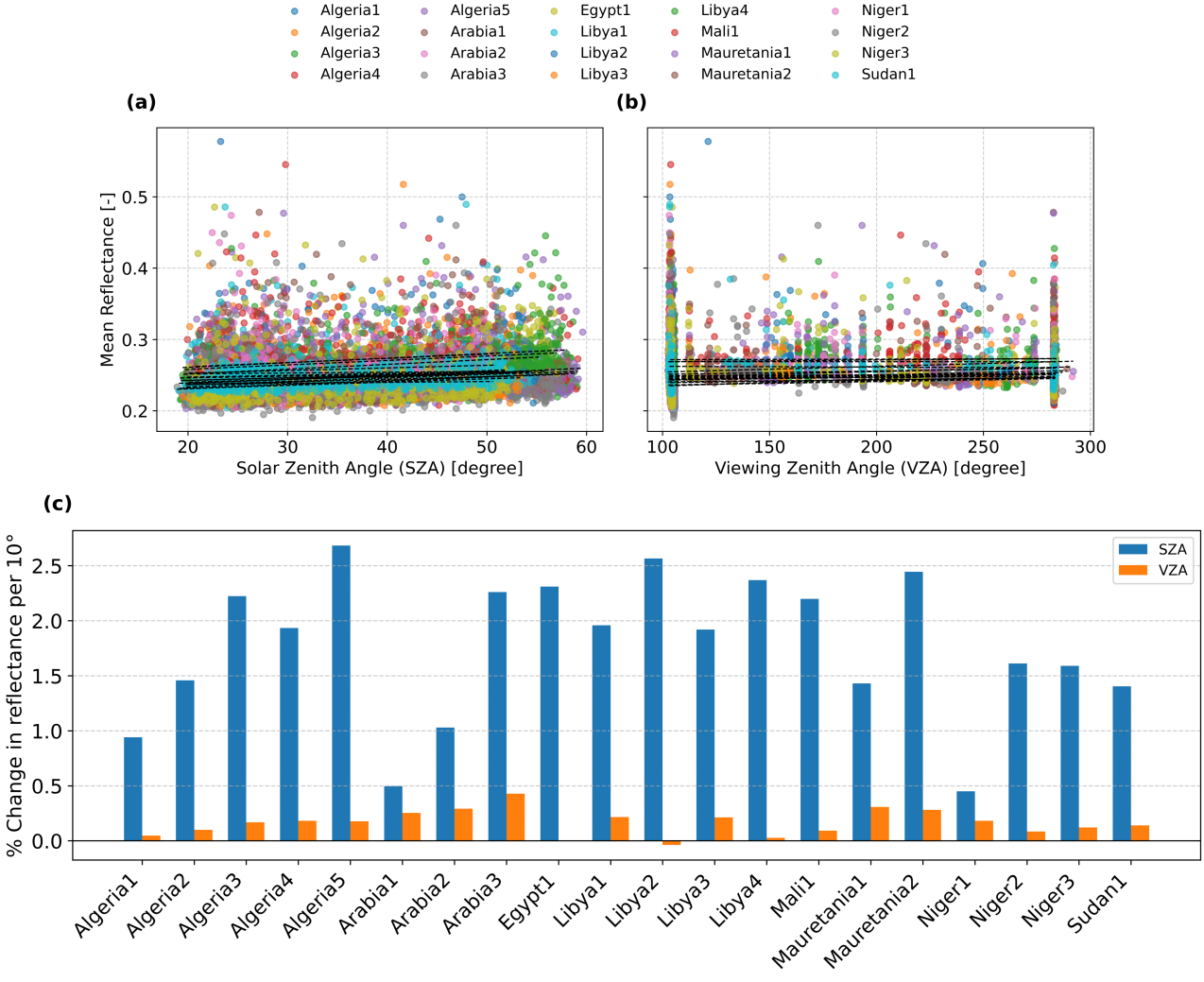

Figure 10. Mean reflectance of the whole spectrum of the PICS observations with respect to SZA and VZA. The scatterplot of the mean reflectance vs (a) SZA, (b) VZA. The fitted linear regression equations for the samples are shown in the black dashed lines (c) the percentage of the changes in mean reflectance per 10 ° changes in SZA (blue bars) and VZA (orange bars).

https://doi.org/10.5194/egusphere-2025-4639
Preprint. Discussion started: 6 October 2025

5.5 Stability score for PICS

The SS for the PICS sites were computed based on SCIAMACHY reflectance observations. The SS was calculated for each spectral channel, excluding O_2 A-band. The scores were normalized and visualized in Fig. 11 with lower values indicating greater stability.

Some sites demonstrated stable performance across nearly all spectral channels. With the most stable sites being Sudan1, Arabia2, and Libya4. In contrast, other sites showed differences when comparing the stability of the different spectral bands. For instance, Arabia3, Arabia2, Libya3, and Niger2 showed higher stability in the UV band compared to the VIS band. Conversely, sites such as Algeria1, Algeria2, Algeria3, Libya4, and Sudan1 demonstrated greater stability in the VIS band than in the UV. A few sites, including Mali1, Mauritania1, Mauritania2, and Niger1 displayed generally low stability across all spectral regions. Additionally, high SS values were observed across multiple sites, appearing as vertically homogeneous patterns. This effect was particularly pronounced in the UV spectral region, likely due to the strong sensitivity of UV bands to atmospheric influences, such as cloud contamination.

The average of the SS for the bands was computed based on the SS of the respective spectral channels. The sites were sorted based on the stability of the bands in Fig. A2 in the appendix. The average SS for each site, including all spectral channels, was presented in Fig. 12. The Sudan1 site had the most stable number of spectral channels, followed by Arabia2 and Libya4.

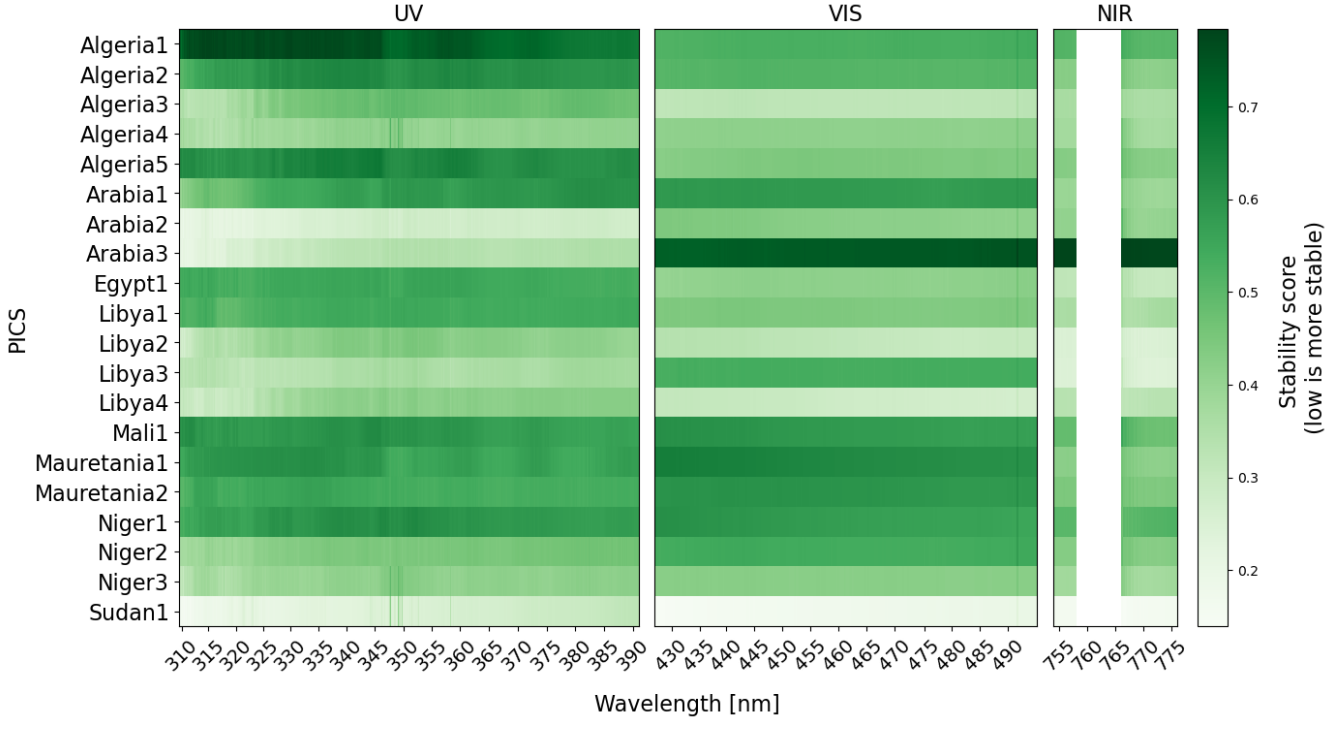

Figure 11. The heatmap of the SS of each wavelength of UV, VIS, and NIR spectral channels. The red dashed lines refer to the boundaries between the channels. The O_2 A-band is excluded from SS computation.

https://doi.org/10.5194/egusphere-2025-4639
Preprint. Discussion started: 6 October 2025

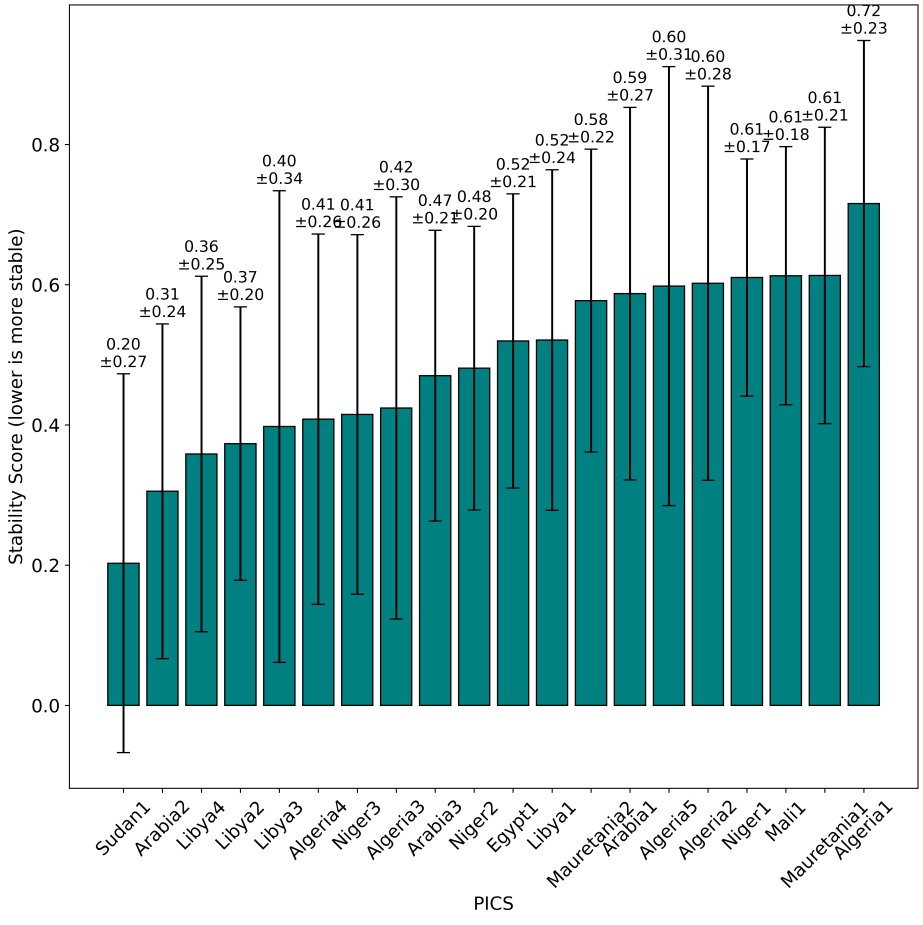

Figure 12. The average of the SS presented in Fig. 11. The SS and the standard deviation of each PICS are shown.

https://doi.org/10.5194/egusphere-2025-4639
Preprint. Discussion started: 6 October 2025

6 Discussion

6.1 Framework

To ensure the robustness and comprehensive assessment of the reflectance time series and the comparison between sensors, additional statistical descriptors were included. Besides the basic statistical parameters and CV, other parameters like IQR, slope, skewness, and kurtosis were included in the assessment. Skewness, kurtosis, and IQR parameters were used to identify the level of symmetry in the observations, reflect the presence of outliers, and quantify the spread of the central portion of the data. Furthermore, the slope was an indicator of the degradation in the sensor performance.

With only basic statistical parameters (mean, standard deviation, and CV), there were no significant differences observed for the spectrometer samples. When additional parameters such as slope, skewness, and kurtosis were considered, meaningful differences became apparent (see Fig. 9). These high-order statistical features provided greater sensitivity to distributional characteristics, subtle anomalies, and temporal trends, thereby offering a more robust basis for distinguishing the performance and stability of the spectrometers. This multi-parameter approach contributed to a more robust and resilient framework for sensor performance evaluation, radiometer drift monitoring, and identifying the constrained and reference sensors for cross-calibration.

6.2 Reflectance time series

The derived indicators from the reflectance time series of GOME and SCIAMACHY revealed different statistical patterns among the PICS and across spectral channels. The spectral behaviour of different PICS was different, suggesting that the initial hypothesis—that all PICS should behave similarly—was not entirely accurate. Therefore, PICS should be regularly investigated (Tuli et al., 2019). This finding underscored the need to quantify and compare the stability of each PICS site individually and across different spectral bands. Moreover, measurements of both spectrometers showed that the stability depends on the spectral band. In particular, for many sites, the VIS band demonstrated higher stability compared to UV. The VIS band is less affected by atmospheric processes, which makes the VIS inherently more stable. The UV is highly sensitive to atmospheric effects such as ozone absorption, aerosol scattering, and contamination. The aerosols could strongly affect short wavelengths (Thome, 2001). These findings underscore the need for a careful, site- and band-specific assessment when selecting PICS for cross-calibration purposes.

6.3 Comparative analysis of GOME vs. SCIAMACHY

To quantitatively assess the stability of the PICS, it was crucial to first determine which satellite sensor provided more reliable and consistent observations. A comparative analysis of key statistical parameters revealed that SCIAMACHY exhibited more statistically uniform and stable reflectance measurements than GOME. These indicators suggested lower temporal variability and fewer extreme values in SCIAMACHY data, making it a more robust choice. (Noël et al., 2007) investigated the degradation across the spectral channels of SCIAMACHY and found that even after reaching the nominal lifetime of the mission in 2007,

https://doi.org/10.5194/egusphere-2025-4639
Preprint. Discussion started: 6 October 2025

the SCIAMACHY instrument was still in good condition. However, the same study demonstrated an increased degradation in UV channels.

The discrepancy in the derived statistical parameters between GOME and SCIAMACHY might be partly attributed to sensor degradation effects. (Lieuwe G Tilstra and Stammes, 2006; Coldewey-Egbers et al., 2008) referred to the severe degradation of the GOME instrument in the UV due to scan mirror degradation. Our findings for the UV of the Libya4 site in Fig. 3 showed an unexpected pattern in reflectance for the observation dates from 2001. Overall, SCIAMACHY's enhanced design and calibration capabilities resulted in better long-term radiometric stability compared to GOME. (Hilbig et al., 2019; Krijger et al., 2014) presented a degradation correction approach based on SCIAMACHY's internal white light measurements in combination with direct solar measurements. Consequently, SCIAMACHY was adopted as the reference sensor for evaluating the temporal stability of the PICS. Using SCIAMACHY observations in this paper ensured that the derived SS were based on a more stable and consistent dataset, enhancing the reliability of the site rankings and subsequent cross-calibration efforts.

6.4 Refinement reflectance observations for reliable estimation of the stability scores

Two additional preprocessing steps were applied before computing the SS. The first involved the exclusion of the O_2 A-band, as the derived metric parameters indicated instability in this spectral region across most sites (see Fig. 8). The second step examined the influence of solar illumination and satellite viewing geometry on the observed reflectance. The reflectance observations collected over PICS were found to exhibit varying degrees of dependence on SZA and, to a lesser extent, on the VZA. Overall, most sites experienced changes of approximately 1–2% per 10° variation in SZA and about 0.5% per 10° variation in VZA. This dependence on SZA is consistent with previous findings; for instance, (Wang et al., 2022) reported that reflectance tends to increase with both the atmospheric aerosol optical depth and SZA. Similarly, (Kim et al., 2023) parameterized the surface reflectance for the geostationary imager of the Moderate Resolution Imaging Spectroradiometer (MODIS), demonstrating that surface reflectance in the blue and visible spectral ranges was linearly proportional to SZA. These results suggest that a portion of the observed reflectance variability can be attributed to the sensitivity of surface reflectance to changes in SZA. Accounting for this effect is therefore essential when analyzing temporal reflectance patterns or performing cross-sensor calibration. However, the overall influence of SZA and VZA on reflectance variation was not significant.

6.5 Stability of PICS

SS served as an indicator of temporal variability across the spectral channels. The SSs for PICS were estimated based on groups of parameters that directly quantified variability, distribution, and temporal trends. The features describing temporal variability in reflectance were normalized to ensure comparability across sites. Furthermore, the normalization prevented large numerical ranges from dominating the magnitude of the SS.

The results demonstrated a wide range of SS across spectral bands and sites. Our findings confirmed that Libya4—one of the recommended sites for sensor cross-calibration—was among the most stable PICS. Some sites, such as Sudan1 and Arabia2, exhibited even higher scores than Libya4. These three sites are, therefore, recommended for further cross-calibration activities.

https://doi.org/10.5194/egusphere-2025-4639
Preprint. Discussion started: 6 October 2025

A flip in stability performance was observed across sites. Arabia3 and Niger2 were more stable in the UV than VIS, while Algeria3 and Algeria5 showed the opposite. Most PICS exhibited higher stability in the NIR—excluding the O_2 A-band—compared to UV and VIS.

Differing SS across the PICS could refer to the following reasons:

- Surface characteristics:

  Site properties affect radiometric stability; PICS are not fully invariant. Relevant factors include sand topography, grain size (Niro et al., 2021), composition, color, material type, and dune displacement (Govaerts, 2015). The sun's azimuth relative to dune alignment influences reflectance, with mean values depending on the area size (Govaerts, 2015).

- Meteorological conditions:

  Strong winds and pressure can transport dust over large areas. Saharan dust storms in June 2020 caused high aerosol optical depths to extend to the USA within 4 days (Francis et al., 2020). Such events particularly affect short wavelengths (blue/visible) due to aerosol scattering.

7 Conclusion

This paper presented a statistical framework based on multiple indicators to compare different sensors, monitor sensor performance, identify sensor-related issues, determine reference and constrained sensors for cross-calibration over PICS, and investigate the temporal variability of spectral bands and PICS. The framework incorporated a wide range of parameters, including traditional time series metrics such as the mean, standard deviation, and CV. In addition, it includes additional indicators that provide insights into the distribution shape of observations, the presence of anomalies, and temporal trends.

The GOME and SCIAMACHY spectrometers were used in this study due to their similar sensor characteristics and mission objectives, as well as overlapping spectral coverage. Additionally, their missions provided approximately 10 years of overlapping observation data, with a temporal offset of about 30 minutes in their overpass times. A decade of reflectance measurements from both sensors was retrieved under nearly clear-sky conditions over PICS.

The results highlighted instrumental issues in GOME, including significant degradation observed in 2001 and irregular observation patterns toward the end of its operational life. These findings agreed with previous studies that reported pronounced degradation of GOME, particularly in the UV spectral band. Moreover, statistical indicators revealed high positive values of skewness and kurtosis, indicating an asymmetrical distribution and the presence of numerous outliers. In contrast, SCIAMACHY observations were found to be more uniform and stationary, with substantially lower trends compared to GOME. As a result, SCIAMACHY was considered the reference sensor in this study for assessing the stability of PICS.

In terms of site stability, areas larger than the spatial extension of PICS were considered, due to the large footprint of the spectrometers. Furthermore, this study aims to establish a foundation for spectrometer cross-calibration, for which the temporal stability of areas larger than the PICS is a critical factor. The analysis revealed considerable variation among the PICS. While some sites exhibited high temporal stability across all spectral channels, others showed inconsistent behavior across bands, and

https://doi.org/10.5194/egusphere-2025-4639
Preprint. Discussion started: 6 October 2025

a subset of sites displayed significantly lower stability, up to two to three times less stable than the most consistent sites. These findings emphasize the importance of selecting suitable PICS for radiometric calibration, taking into account the spectral band of interest. Furthermore, periodic evaluation of these sites is crucial to ensure their long-term stability. The proceeding paper will perform the cross-calibration of GOME and SCIAMACHY based on the most stable sites.

https://doi.org/10.5194/egusphere-2025-4639
Preprint. Discussion started: 6 October 2025

Data availability. SCIAMACHY Level 1b: https://doi.org/10.5270/EN1-5eab12a
SCIAMACHY 1c tool: https://earth.esa.int/eogateway/tools/scial1c-command-line-tool
GOME-1 Level 1b: https://earth.esa.int/eogateway/instruments/gome/products-information
FDR4ATMOS products: https://doi.org/10.5270/ESA-852456e

Author contributions. **Owda**: Conceptualization, Methodology, Programming, Investigation, Writing—original draft. **Lichtenberg**: Writing—review & editing.

Competing interests. The authors declare no competing financial or personal interests that could have influenced this work.

Acknowledgements. The FDR4ATMOS project, initiated by ESA, provides long-term records of Earth observation Level 1 parameters (radiance, irradiance, reflectance) to improve the performance of mission datasets (https://atmos.eoc.dlr.de/FDR4ATMOS/, accessed 20 September 2025).

https://doi.org/10.5194/egusphere-2025-4639
Preprint. Discussion started: 6 October 2025

A Appendix A

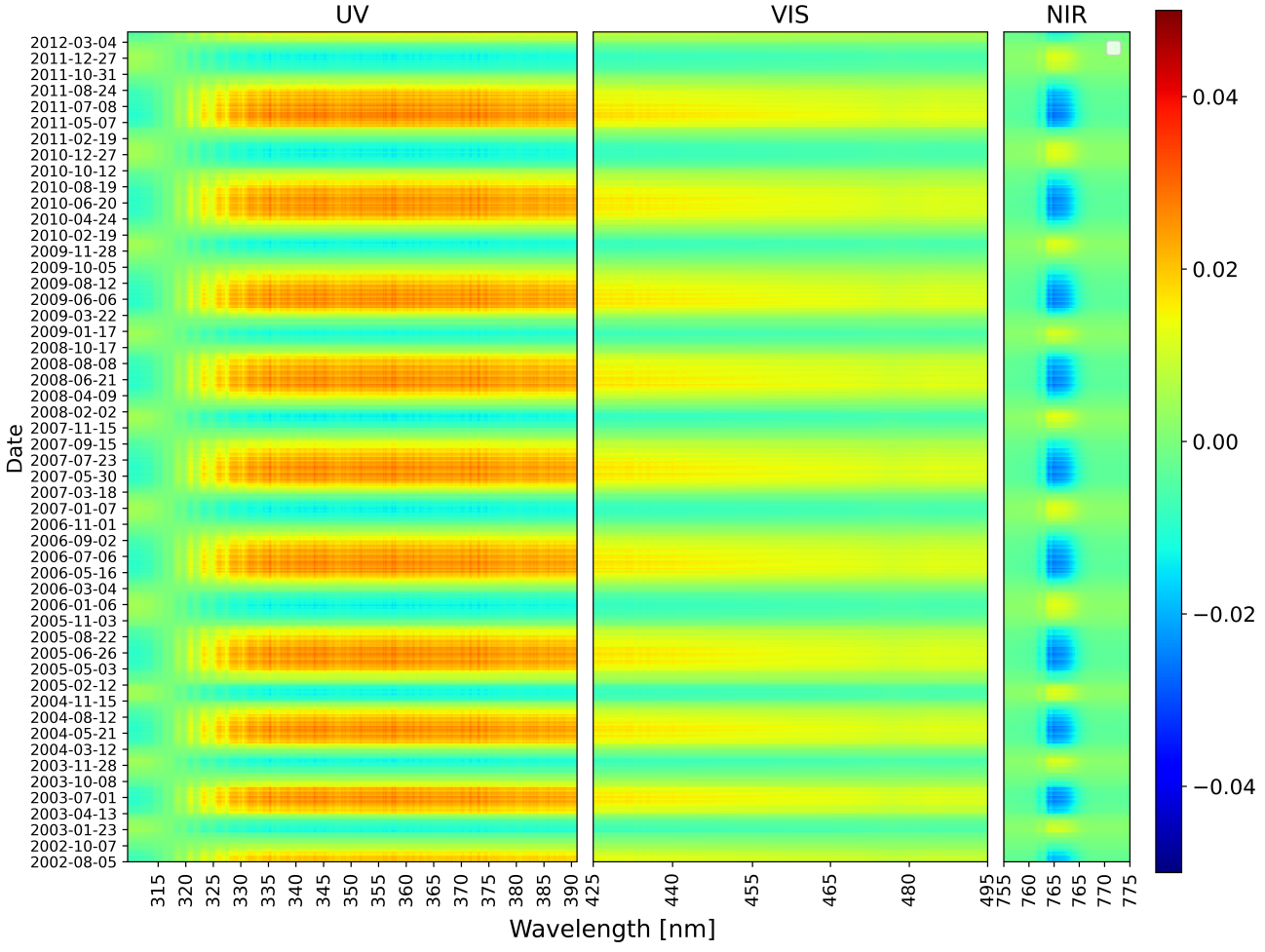

Figure A1. Heatmap of the difference in the reflectance observations of the Libya4 site. The difference was calculated based on the equation R_{corr} - R (corrected-original)

https://doi.org/10.5194/egusphere-2025-4639
Preprint. Discussion started: 6 October 2025

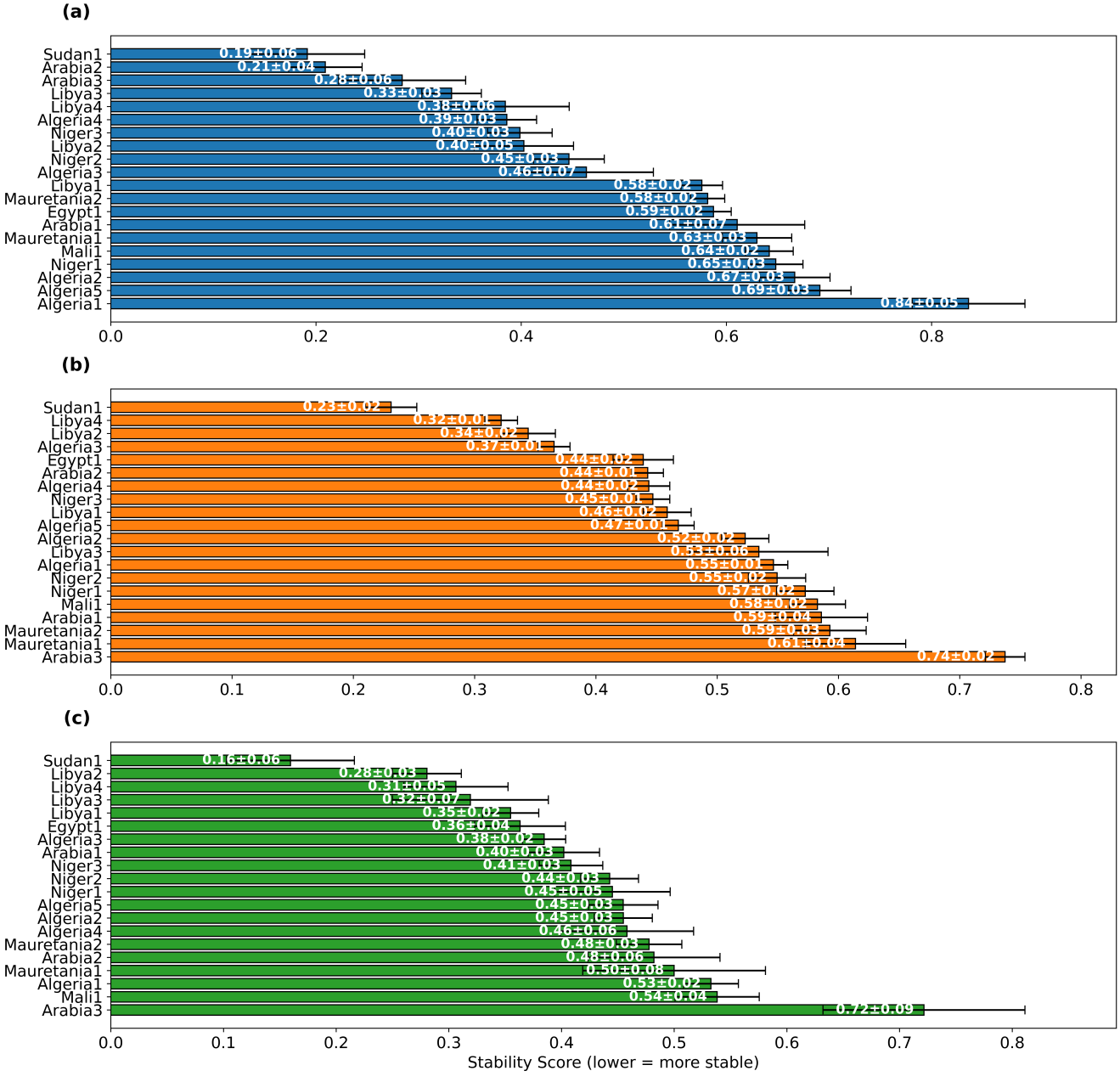

Figure A2. Ranking of PICS based on the SS of the bands: (a) UV, (b) VIS, and (c) NIR.

https://doi.org/10.5194/egusphere-2025-4639
Preprint. Discussion started: 6 October 2025

Table A1. PICS sites along with their geographic coordinates and the number of collocations identified at each site for both spectrometers.

PICS	Center longitude [○]	Center latitude [○]	Number of observations SCIAMACHY	Number of observations GOME
Arabia1	46.76	18.88	548	519
Arabia2	50.96	20.13	562	453
Arabia3	43.73	28.92	563	468
Sudan1	28.22	21.74	565	979
Niger1	9.81	19.67	579	927
Niger2	10.59	21.37	562	708
Niger3	7.96	21.57	570	983
Egypt1	26.10	27.12	553	818
Libya1	13.35	24.42	551	737
Libya2	20.48	25.05	579	845
Libya3	23.10	23.15	569	704
Libya4	23.39	28.55	568	716
Algeria1	-0.40	23.80	554	687
Algeria2	-1.38	26.09	528	802
Algeria3	7.66	30.32	525	839
Algeria4	5.59	30.04	556	839
Algeria5	2.23	31.02	436	830
Mali1	-4.85	19.12	523	905
Mauretania1	19.40	19.40	502	656
Mauretania2	20.85	20.85	543	947

https://doi.org/10.5194/egusphere-2025-4639
Preprint. Discussion started: 6 October 2025

References

Barsi, Julia A, Bahjat Alhammoud, Jeffrey Czapla-Myers, Ferran Gascon, Md Obaidul Haque, Morakot Kaewmanee, Larry Leigh, and Brian L Markham (2018). "Sentinel-2A MSI and Landsat-8 OLI radiometric cross comparison over desert sites". In: *European Journal of Remote Sensing* 51.1, pp. 822–837. DOI: https://doi.org/10.1080/22797254.2018.1507613.

Bovensmann, Heinrich, JP Burrows, M Buchwitz, Johannes Frerick, Suresh Noel, VV Rozanov, KV Chance, and APH Goede (1999). "SCIAMACHY: Mission objectives and measurement modes". In: *Journal of the atmospheric sciences* 56.2, pp. 127–150.

Burrows, John P, Mark Weber, Michael Buchwitz, Vladimir Rozanov, Annette Ladstätter-Weißenmayer, Andreas Richter, Rüdiger DeBeek, Ricarda Hoogen, Klaus Bramstedt, Kai-Uwe Eichmann, et al. (1999). "The global ozone monitoring experiment (GOME): Mission concept and first scientific results". In: *Journal of the Atmospheric Sciences* 56.2, pp. 151–175.

Cabor, F, Olivier Hagolle, HCLKNE Cosnefroy, and Xavier Briottet (1998). "Inter-calibration using desertic sites as a reference target". In: *IGARSS'98. Sensing and Managing the Environment. 1998 IEEE International Geoscience and Remote Sensing. Symposium Proceedings.(Cat. No. 98CH36174)*. Vol. 5. IEEE, pp. 2713–2715. DOI: 10.1109/IGARSS.1998.702327.

Chander, Gyanesh, Tim J Hewison, Nigel Fox, Xiangqian Wu, Xiaoxiong Xiong, and William J Blackwell (2013). "Overview of intercalibration of satellite instruments". In: *IEEE Transactions on Geoscience and Remote Sensing* 51.3, pp. 1056–1080. DOI: 10.1109/TGRS.2012.2228654.

Coldewey-Egbers, Melanie, Sander Slijkhuis, Bernd Aberle, and Diego Loyola (2008). "Long-term analysis of GOME in-flight calibration parameters and instrument degradation". In: *Applied Optics* 47.26, pp. 4749–4761. DOI: DOI:10.1364/ao.47.004749.

Cosnefroy, Hélène, Marc Leroy, and Xavier Briottet (1996). "Selection and characterization of Saharan and Arabian desert sites for the calibration of optical satellite sensors". In: *Remote Sensing of Environment* 58.1, pp. 101–114. ISSN: 0034-4257. DOI: https://doi.org/10.1016/0034-4257(95)00211-1. URL: https://www.sciencedirect.com/science/article/pii/0034425795002111.

ESA (2025a). *Global Ozone Monitoring Experiment (GOME)*. URL: https://earth.esa.int/eogateway/instruments/gome (visited on 09/11/2025).

– (2025b). *SCIAMACHY Instrument Overview*. URL: https://earth.esa.int/eogateway/instruments/sciamachy (visited on 09/11/2025).

Fajardo Rueda, Juliana, Larry Leigh, Cibele Teixeira Pinto, Morakot Kaewmanee, and Dennis Helder (2021). "Classification and Evaluation of Extended PICS (EPICS) on a Global Scale for Calibration and Stability Monitoring of Optical Satellite Sensors". In: *Remote Sensing* 13.17, p. 3350. DOI: https://doi.org/10.3390/rs13173350.

Francis, Diana, Ricardo Fonseca, Narendra Nelli, Juan Cuesta, Michael Weston, Amato Evan, and Marouane Temimi (2020). "The atmospheric drivers of the major Saharan dust storm in June 2020". In: *Geophysical Research Letters* 47.24, e2020GL090102. DOI: 10.1029/2020GL090102.

Govaerts, Yves M (2015). "Sand dune ridge alignment effects on surface BRF over the Libya-4 CEOS calibration site". In: *Sensors* 15.2, pp. 3453–3470. DOI: https://doi.org/10.3390/s150203453.

Han, J., J. Pei, and H. Tong (2022). *Data Mining: Concepts and Techniques*. The Morgan Kaufmann Series in Data Management Systems. Morgan Kaufmann. ISBN: 9780128117613. URL: https://books.google.de/books?id=NR1oEAAAQBAJ.

Hasan, Md Nahid, Mahesh Shrestha, Larry Leigh, and Dennis Helder (2019). "Evaluation of an Extended PICS (EPICS) for calibration and stability monitoring of optical satellite sensors". In: *Remote Sensing* 11.15, p. 1755. DOI: https://doi.org/10.3390/rs11151755.

https://doi.org/10.5194/egusphere-2025-4639
Preprint. Discussion started: 6 October 2025

Helder, Dennis, Kurtis J Thome, Nischal Mishra, Gyanesh Chander, Xiaoxiong Xiong, Amit Angal, and Taeyoung Choi (2013). "Absolute radiometric calibration of Landsat using a pseudo invariant calibration site". In: *IEEE Transactions on Geoscience and Remote Sensing* 51.3, pp. 1360–1369.

Hilbig, Tina, Klaus Bramstedt, Mark Weber, John P Burrows, and Matthijs Krijger (2019). "Optimised degradation correction for SCIAMACHY satellite solar measurements from 330 to 1600 nm by using its internal white light source". In: *Atmospheric Measurement Techniques Discussions* 2019, pp. 1–23. DOI: https://doi.org/10.5194/amt-13-3893-2020.

Kabir, Sakib, Larry Leigh, and Dennis Helder (2020). "Vicarious methodologies to assess and improve the quality of the optical remote sensing images: A critical review". In: *Remote Sensing* 12.24, p. 4029. DOI: https://doi.org/10.3390/rs12244029.

Khadka, Neha, Cibele Teixeira Pinto, and Larry Leigh (2021). "Detection of change points in pseudo-invariant calibration sites time series using multi-sensor satellite imagery". In: *Remote Sensing* 13.11, p. 2079. DOI: https://doi.org/10.3390/rs13112079.

Kim, Mijin, Robert C Levy, Lorraine A Remer, Shana Mattoo, and Pawan Gupta (2023). "Parameterizing spectral surface reflectance relationships for the Dark Target aerosol algorithm applied to a geostationary imager". In: *Atmospheric Measurement Techniques Discussions* 2023, pp. 1–42. DOI: https://doi.org/10.5194/amt-17-1913-2024.

Krijger, JM, R Snel, G Van Harten, JHH Rietjens, and I Aben (2014). "Mirror contamination in space I: mirror modelling". In: *Atmospheric Measurement Techniques* 7.10, pp. 3387–3398. DOI: https://doi.org/10.5194/amt-7-3387-2014.

Lacherade, Sophie, Bertrand Fougnie, Patrice Henry, and Philippe Gamet (2013). "Cross calibration over desert sites: Description, methodology, and operational implementation". In: *IEEE Transactions on Geoscience and Remote Sensing* 51 (3), pp. 1098–1113. ISSN: 01962892. DOI: 10.1109/TGRS.2012.2227061.

Liang, Shunlin (2017). *Comprehensive remote sensing*. Elsevier.

Lichtenberg, G, Q Kleipool, JM Krijger, G Van Soest, R Van Hees, LG Tilstra, JR Acarreta, I Aben, B Ahlers, H Bovensmann, et al. (2006). "SCIAMACHY Level 1 data: calibration concept and in-flight calibration". In: *Atmospheric Chemistry and Physics* 6.12, pp. 5347–5367. DOI: https://doi.org/10.5194/acp-6-5347-2006.

Niro, Fabrizio, Philippe Goryl, Steffen Dransfeld, Valentina Boccia, Ferran Gascon, Jennifer Adams, Britta Themann, Silvia Scifoni, and Georgia Doxani (2021). "European Space Agency (ESA) calibration/validation strategy for optical land-imaging satellites and pathway towards interoperability". In: *Remote Sensing* 13.15, p. 3003. DOI: https://doi.org/10.3390/rs13153003.

Noël, Stefan, Klaus Bramstedt, Heinrich Bovensmann, John P Burrows, Manfred Gottwald, and Eckhart Krieg (2007). "SCIAMACHY degradation monitoring results". In: *Proceedings of the 2007 Envisat Symposium*. Citeseer.

Ono, Akira, Fumihiro Sakuma, Kohei Arai, Y Yamaguchi, H Fujisada, PN Slater, KJ Thome, Frank Don Palluconi, and HH Kieffer (1996). "Preflight and in-flight calibration plan for ASTER". In: *Journal of Atmospheric and Oceanic Technology* 13.2, pp. 321–335. DOI: https://doi.org/10.1175/1520-0426(1996)013<0321:PAIFCP>2.0.CO;2.

Pagano, Thomas S, Hartmut H Aumann, Denise E Hagan, and Ken Overoye (2003). "Prelaunch and in-flight radiometric calibration of the Atmospheric Infrared Sounder (AIRS)". In: *IEEE transactions on geoscience and remote sensing* 41.2, pp. 265–273. DOI: 10.1109/TGRS.2002.808324.

Thenkabail, Prasad S (2015). *Remotely sensed data characterization, classification, and accuracies*. CRC press.

Thome, KJ (2001). "Absolute radiometric calibration of Landsat 7 ETM+ using the reflectance-based method". In: *Remote Sensing of Environment* 78.1-2, pp. 27–38. DOI: https://doi.org/10.1016/S0034-4257(01)00247-4.

Tilstra, Lieuwe G and Piet Stammes (2006). "Intercomparison of reflectances observed by GOME and SCIAMACHY in the visible wavelength range". In: *Applied optics* 45.17, pp. 4129–4135. DOI: 10.1364/ao.45.004129.

https://doi.org/10.5194/egusphere-2025-4639
Preprint. Discussion started: 6 October 2025

Tuli, Fatima Tuz Zafrin, Cibele Teixeira Pinto, Amit Angal, Xiaoxiong Xiong, and Dennis Helder (2019). "New approach for temporal stability evaluation of pseudo-invariant calibration sites (PICS)". In: *Remote Sensing* 11.12, p. 1502.

Wang, Weile, Yujie Wang, Alexei Lyapustin, Hirofumi Hashimoto, Taejin Park, Andrew Michaelis, and Ramakrishna Nemani (2022). "A novel atmospheric correction algorithm to exploit the diurnal variability in hypertemporal geostationary observations". In: *Remote Sensing* 14.4, p. 964. DOI: https://doi.org/10.3390/rs14040964.

Wu, A, Q Mu, A Angal, and X Xiong (2020). "Assessment of MODIS and VIIRS calibration consistency for reflective solar bands calibration using vicarious approaches". In: *Sensors, Systems, and Next-Generation Satellites XXIV*. Vol. 11530. SPIE, pp. 235–246.

Ye, Xin, Huazhong Ren, Yanzhen Liang, Jinshun Zhu, Jinxin Guo, Jing Nie, Hui Zeng, Yanhua Zhao, and Yonggang Qian (2021). "Cross-calibration of Chinese Gaofen-5 thermal infrared images and its improvement on land surface temperature retrieval". In: *International Journal of Applied Earth Observation and Geoinformation* 101, p. 102357. DOI: https://doi.org/10.1016/j.jag.2021.102357.